TABLE OF CONTENTS

Chapter 1

INTRODUCTION

This thesis derives the mechanical, fluid and electromagnetic model of a solenoid valve from the structural parameters. TODO: write abstract

Chapter 2

MAGNETO MOTIVE FORCE

Magneto motive force is force that allows solenoid valves to open using the linear motion of an armature. Magneto motive force is a function of magnetic flux ϕ, surface area perpendicular to the magnetic flux acting on armature S_2 and magnetic reluctance of vacuum or material filling range of linear motion μ_0.

$$F_{mag} = \frac{1 \cdot \phi^2}{2 \cdot \mu_0 \cdot S_2} \tag{2.1}$$

2.1 Magnetic Flux

Magnetic flux through the magnetic circuit of a valve is a function of coil turns N, current through the coil I, and total magnetic reluctance of the magnetic circuit R_{total}.

$$\phi = \frac{N \cdot I}{R_{total}} \tag{2.2}$$

N is constrained by the geometry of the valve, there is a limit on how many turns one can add for a given cross sectional area. I is constrained by the wire current carrying capacity. In further section we will analyze the effect of wire diameter and valve geometry on magnetic flux and magneto motive force.

2.1.1 Magnetic Reluctance

Magnetic reluctance R of a simple 430F stainless steel block can be computed as:

$$R = \frac{l}{\mu_0 \mu_r A} \tag{2.3}$$

where l is length of the magnetic path in meters, μ_0 is permeability of free space (vacuum) $4\pi \cdot 10^{-7} H/m$, μ_r is relative permeability of a magnetic material (850 for 430F SS) and A is the cross sectional area in m^2. [Zhao et al., 2017] Zhao et al.
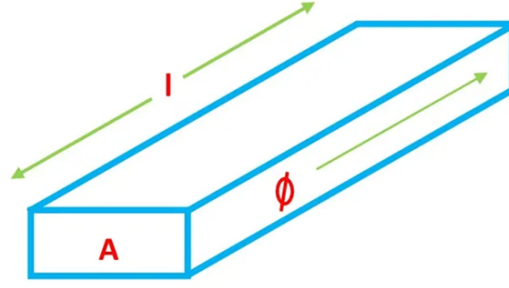
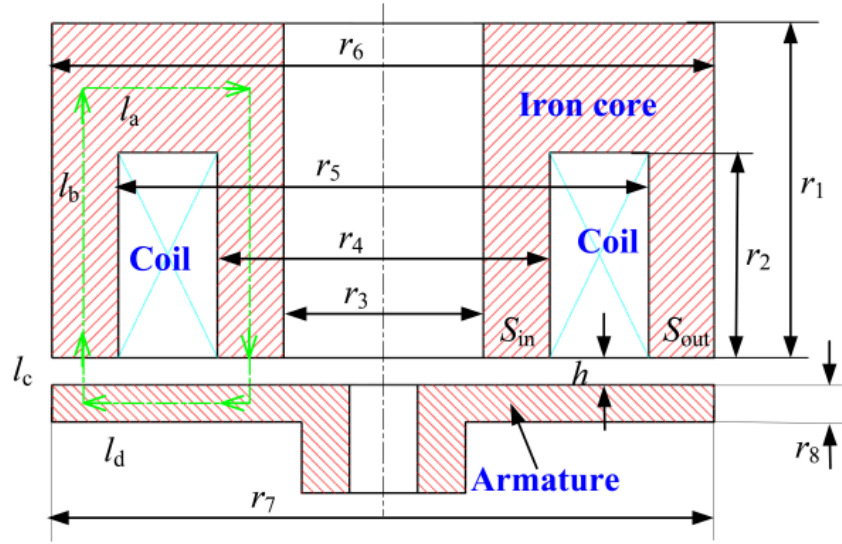Figure 2.1: Magnetic flux through a simple bar

Figure 2.2: The structural schematic of the HSV [Zhao et al., 2017]

studied the effect of structural parameters of a solenoid system with the model: Zhao et al. computed the total magnetic reluctance through the green arrows thus they computed the magnetic flux and magneto motive force. Researchers validated their static electromagnetic force model by running experiments on a test bench where they fixed the armature and the force sensor at one end and placed the iron core free on the other end 2.3. They present the effects of driving current on electromagnetic energy conversion in fig. 2.4. "When I increases from $1A$ to $18A$, the electromagnetic force first increases rapidly, $\partial F/\partial I$ reaches a maximum value at a driving current of $4A$, and then decreases. When $I < 4A$, with increasing I, the increase of the
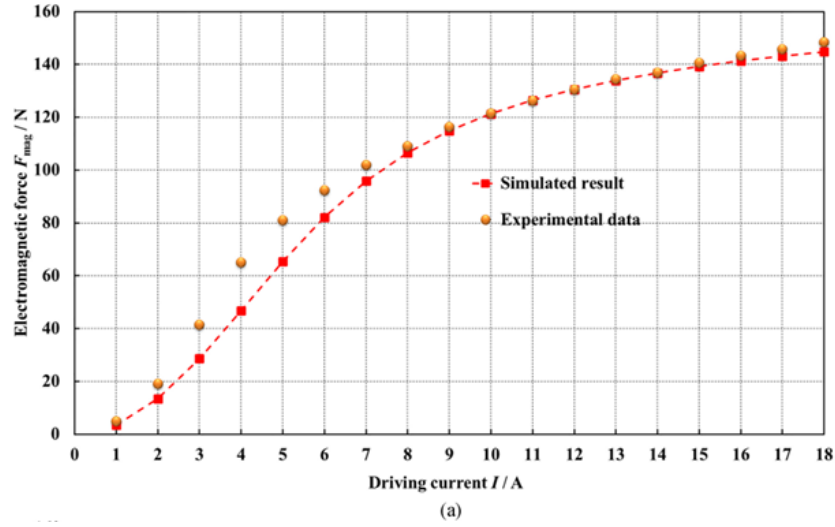
Figure 2.3: Comparison between simulated and experimental results of the electromagnetic force [Zhao et al., 2017]
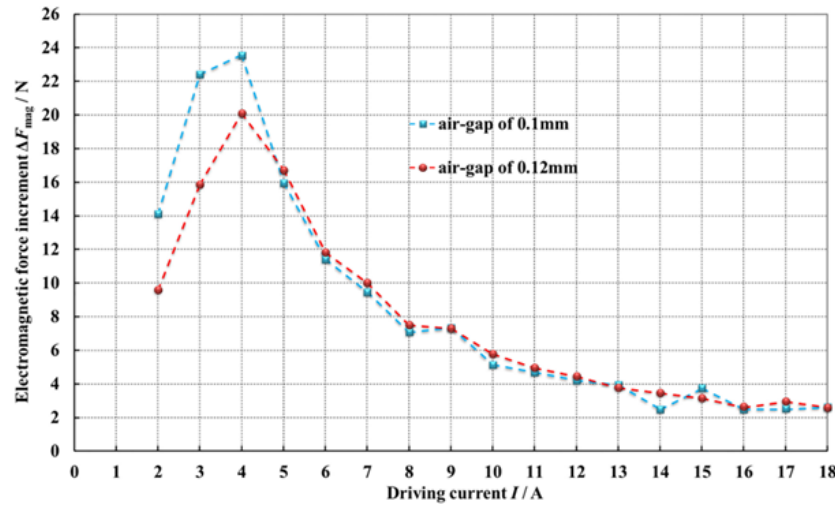

Figure 2.4: Influence of the driving current on the electromagnetic force increment at different working air gaps [Zhao et al., 2017]

electromagnetic force at the air gap of $0.1mm$ always greater than that at the air gap of $0.12mm$. When $I > 4A$, the two curves nearly overlap, and the increment of the electromagnetic force with increasing I gradually decreases. The phenomena can be explained with the B-H curve of the iron core and armature." [Zhao et al., 2017] As seen in fig. 2.5, change $\partial R/\partial I$ starts to dominate the total magnetic reluctance. The researchers conclude that "increasing I will cause premature saturation in the
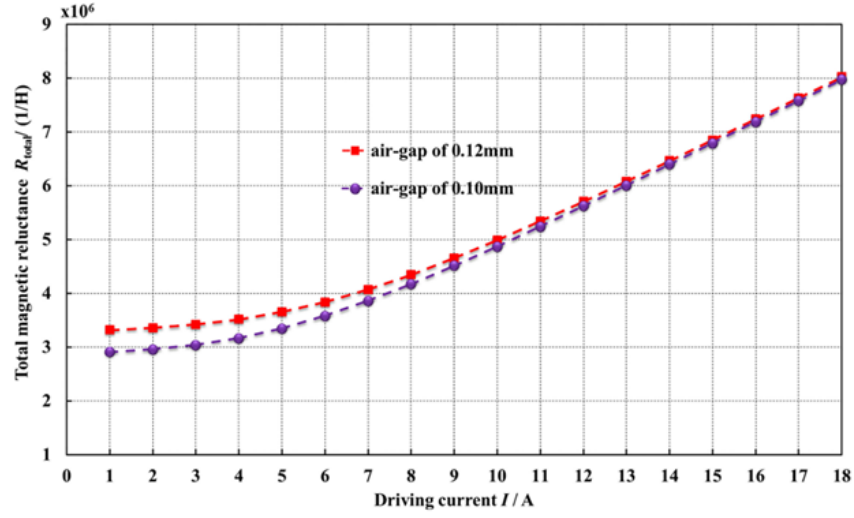
Figure 2.5: Influence of driving current on total magnetic reluctance at different working air gaps [Zhao et al., 2017]

HSV, and the magnetic reluctance of the soft magnetic material will become a decisive factor in restricting the variation of the total magnetic reluctance, which causes the changes of the total magnetic reluctance at different working air gaps to be the same with increasing I. Therefore, it can be surmised that when $I > 4A$, the electromagnetic forces with different working air gaps will increase at the same rate with increasing I."[Zhao et al., 2017] The fig 2.6 show us the B-H curve and
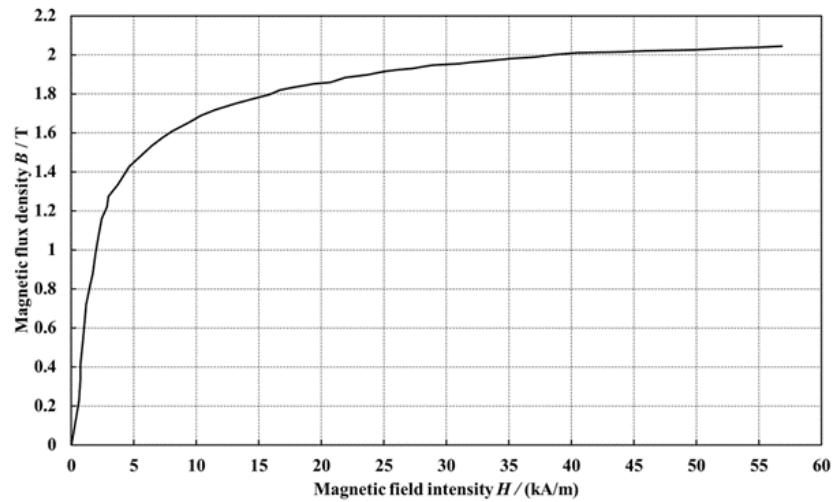

Figure 2.6: The B-H curve of the iron core and armature. [Zhao et al., 2017]

it shows how magnetic saturation occurs. To increase the materials magnetic flux density one must exponentially increase the magnetic field intensity which results in high power consumption or is limited by solenoids current carrying capacity. "I and the working air gap both have significant effects on the variation of the total magnetic reluctance. Too large current or small working air gap will lead to the saturation of magnetic circuit." [Zhao et al., 2017] For an efficient solenoid system the air gap should have the highest magnetic reluctance contribution to the total magnetic reluctance. "Fig 2.7 shows that at different values of I, the electromagnetic
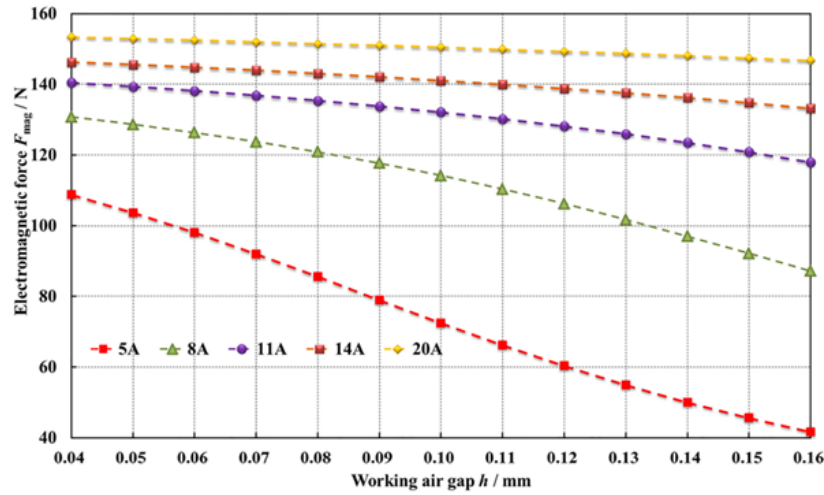

Figure 2.7: Influence of h on the electromagnetic force at different driving currents [Zhao et al., 2017] (x axis is in 10mm)

force decreases with an increasing of the working air gap, and the rate of decrease is affected by the value of I. The larger I becomes, the smaller the rate is." [Zhao et al., 2017] This occurs because the magnetic reluctance caused by saturation is dominates the magnetic reluctance due to the air gap. The fig. 2.8 "shows that at different values of I, the total magnetic reluctance increases with an increase of the working air gap. When the total magnetic flux is constant, the electromagnetic force decreases with increasing total magnetic reluctance. If I is small, the capability of electromagnetic energy conversion in the HSV will be significantly influenced by the working air gap. But if I is large enough to lead to the magnetic saturation, the working air-gap has only a minor influence." [Zhao et al., 2017]
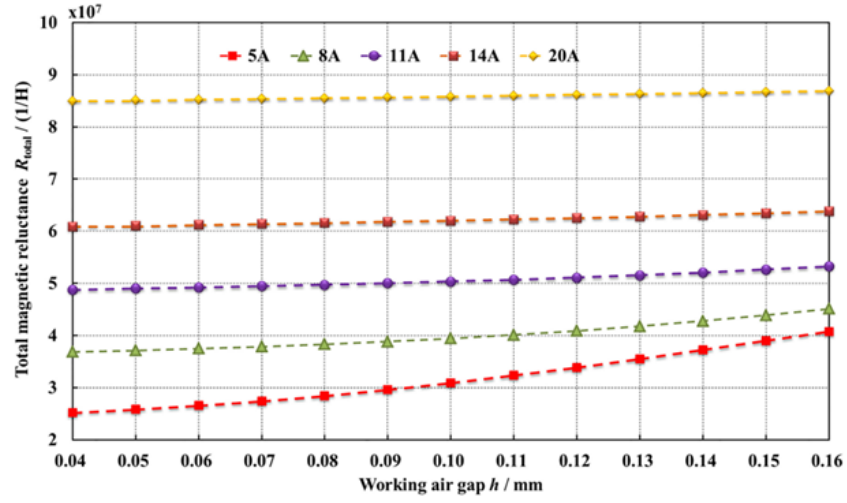
Figure 2.8: Influence of h on the total magnetic reluctance at different driving currents [Zhao et al., 2017] (x axis is in 10mm)
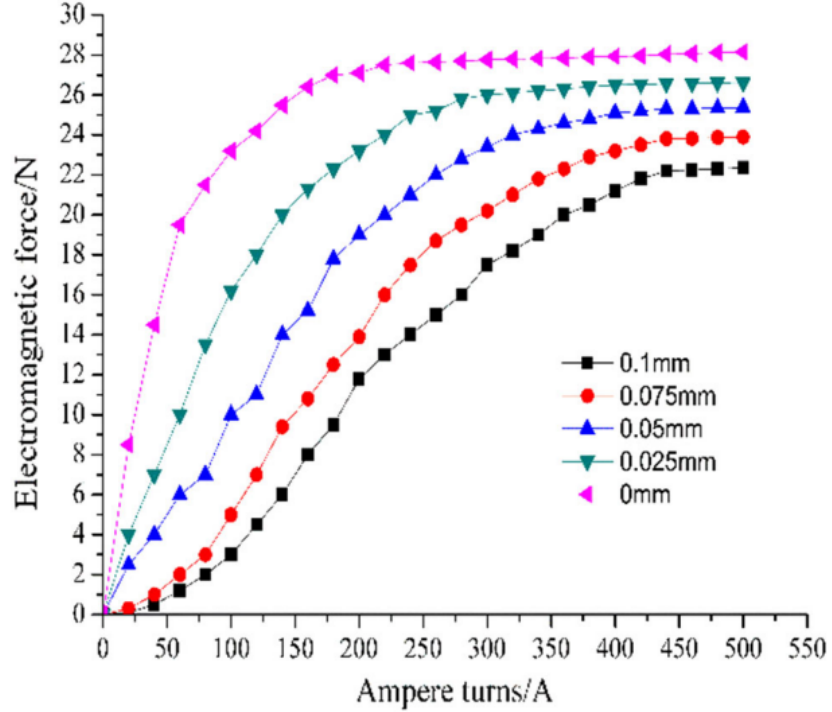
2.1.2 $N \cdot I$ (Ampere Turns)

Figure 2.9: Electromagnetic force of different Ampere-turns [Yang et al., 2019]

As seen in eq. 2.1, magneto motive force is linearly proportional to $N \cdot I$. There

is however a limit to this relationship. In fig. 2.9 Yang et al. shows that magneto motive force is saturated. It should be noted that for different air gaps (range of linear motion) the saturation level varies. Different air gap distances result in exponential increase in air gap magnetic reluctance. thus it requires more ampere turns to increase the magnetic reluctance of the magnetic circuit to match and exceed the air gap.

2.2   Armature Surface Area

Armature surface area perpendicular to the magnetic flux acting on it is crucial in determining magneto motive force as seen in eq. 2.1. Yang et al. improved the efficiency of a micro digital valve by changing the design in such a way that they increased the armature surface area which led to an increase in magnetic flux thus increasing the magneto motive force for the same $N \cdot I$ [Yang et al., 2019]. "Under
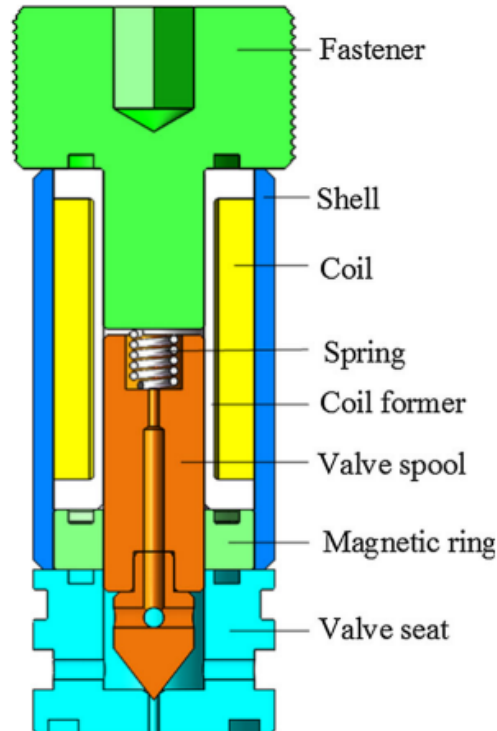
Figure 2.10: Traditional micro high-speed digital valve [Yang et al., 2019]

the same displacement of the iron core, the testing results of electromagnetic force

Figure 2.11: Novel micro high-speed digital valve [Yang et al., 2019]

of the novel micro high-speed digital valve were about 1.33 times as that of the traditional valve. ... ratio of the testing results was in good agreement with the area ratio of the two valves." [Yang et al., 2019]
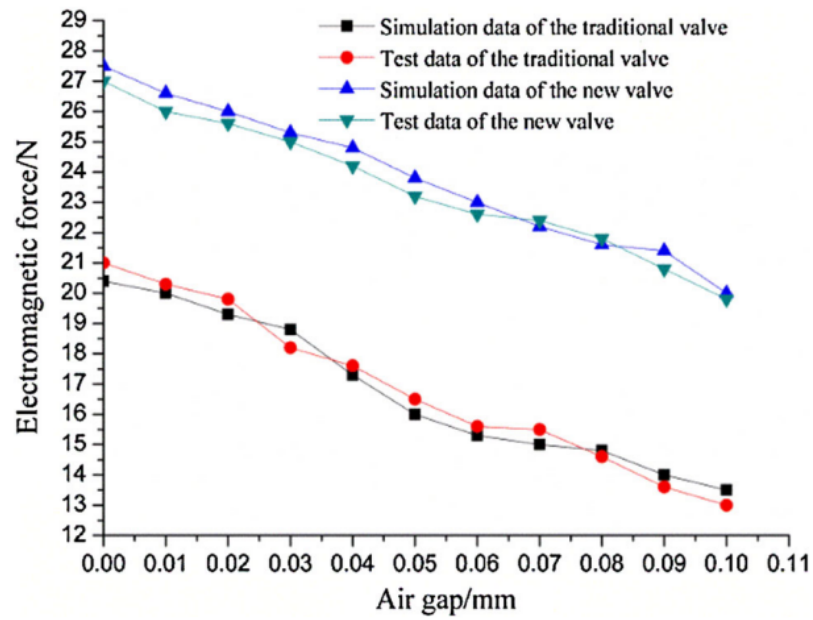
Figure 2.12: Electromagnetic force for different arrangement [Yang et al., 2019]

Chapter 3

MAGNETIC MODEL OF A SOLENOID VALVE

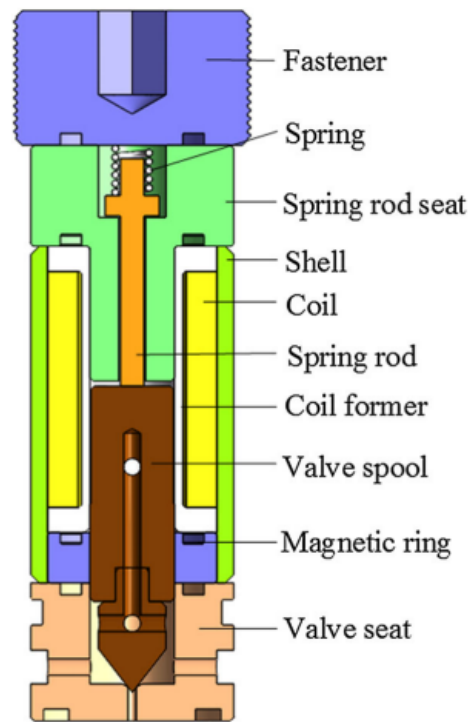In this section we will be modelling the magnetic circuit of the HSV by Yang et al. in the previous chapter. As seen in Fig. 3.1, magnetic circuit is divided in to 4

Figure 3.1: Magnetic path shown on assembly

linear sections following the method of Zhao et al. $Path1$ is uninterrupted and flows through the part labeled as magnetic top.

$$R_{\text{path1}} = \frac{4\,r_{\text{Cout}}}{\mu\,\mu_0\,t_{\text{mta}}\,\pi\,(c_a + c_r + 2\,r_{\text{Cout}} + t_{\text{shell}})} \tag{3.1}$$

Path 2 is divided in to 3 sections. $Path2_a$ is the outer vertical path through the

Figure 3.2: Detail view on vertical air gap between magnetic top and shell.

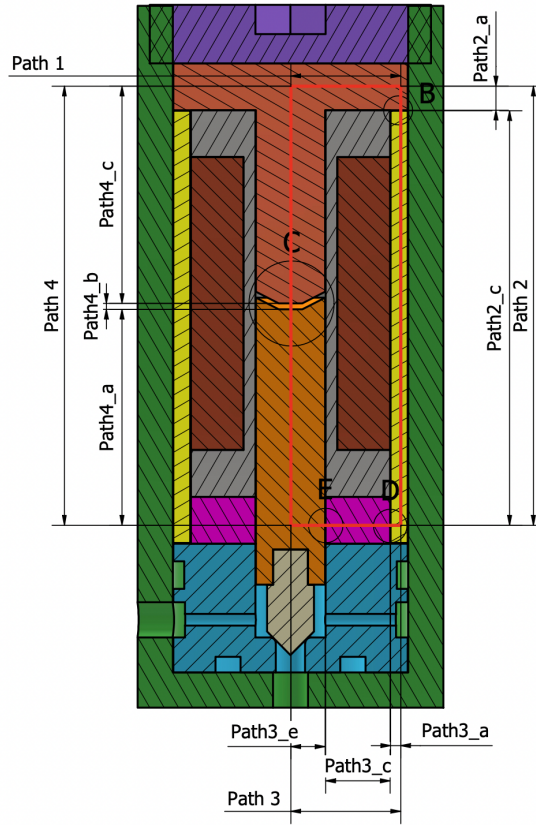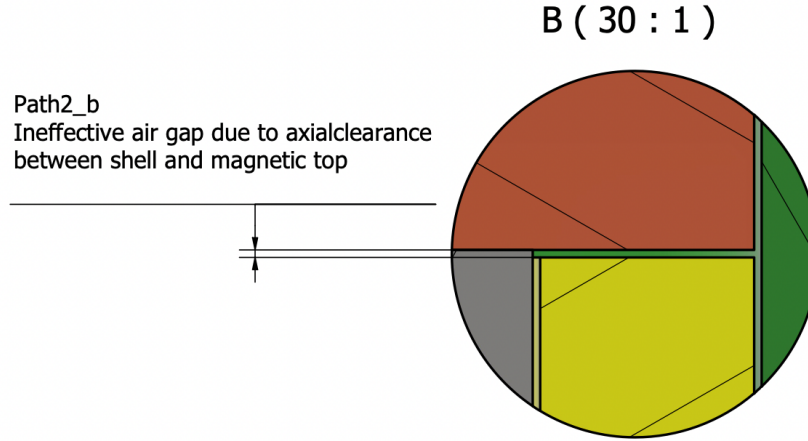magnetic top. $Path2_b$ is the vertical path through the ineffective air gap due to axial clearance between shell and magnetic top shown in Fig. 3.2. $Path2_c$ is the path through shell.

$$R_{\text{path2}} = \frac{c_a}{\mu_0\,\pi\left((c_r + r_{\text{Cout}} + t_{\text{shell}})^2 - (c_r + r_{\text{Cout}})^2\right)} +$$
$$\frac{h_C - c_a + 2\,t_{\text{cfa}} + \frac{t_{\text{mba}}}{2} + t_{\text{mta}}}{\mu\,\mu_0\,\pi\left((c_r + r_{\text{Cout}} + t_{\text{shell}})^2 - (c_r + r_{\text{Cout}})^2\right)} \tag{3.2}$$

Path 3 is divided in to 5 sections. $Path3_a$ is the horizontal path through shell. $Path3_b$ is the path through ineffective air gap due to radial clearance between shell and magnetic bottom shown in Fig. 3.3. $Path3_c$ is the horizontal path through magnetic bottom. $Path3_d$ is the path through ineffective air gap due to radial clearance between shell and magnetic bottom shown in Fig. 3.4. $Path3_e$ is the horizontal path through the armature.

$$R_{\text{path3}} = \frac{2}{\mu\,\mu_0\,t_{\text{mba}}\,\pi} +$$
$$\frac{c_r}{\mu_0\,t_{\text{mba}}\,\pi\left(\frac{c_r}{2} + r_A\right)} +$$
$$\frac{c_r}{\mu_0\,t_{\text{mba}}\,\pi\left(\frac{c_r}{2} + r_{\text{Cout}}\right)} +$$
$$\frac{t_{\text{shell}}}{2\,\mu\,\mu_0\,t_{\text{mba}}\,\pi\left(c_r + r_{\text{Cout}} + \frac{t_{\text{shell}}}{2}\right)} -$$
$$\frac{2\left(c_r + r_A - r_{\text{Cout}}\right)}{\mu\,\mu_0\,t_{\text{mba}}\,\pi\left(c_r + r_A + r_{\text{Cout}}\right)} \tag{3.3}$$

Path 4 is divided in to 3 sections. $Path4_a$ is the vertical path through the armature.

D (30:1)

0,05Path3_b
Ineffective air gap due to radial clearance
between shell and magnetic bottom
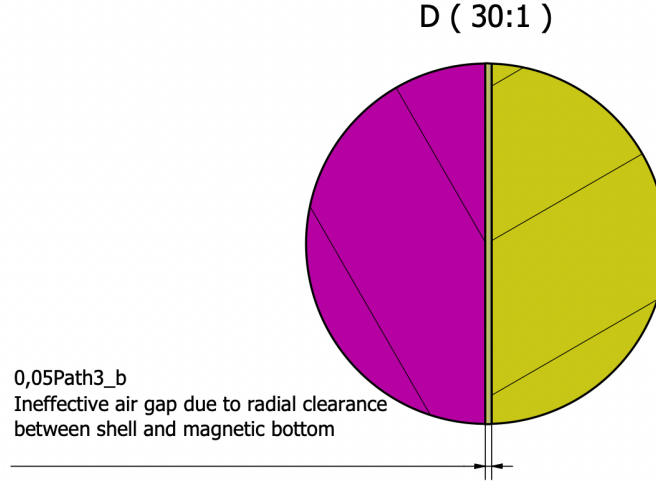
Figure 3.3: Detail view on horizontal air gap between shell and magnetic bottom.

E (30:1)

Path3_d
Ineffective air gap due to radial clearance
between armature and magnetic bottom
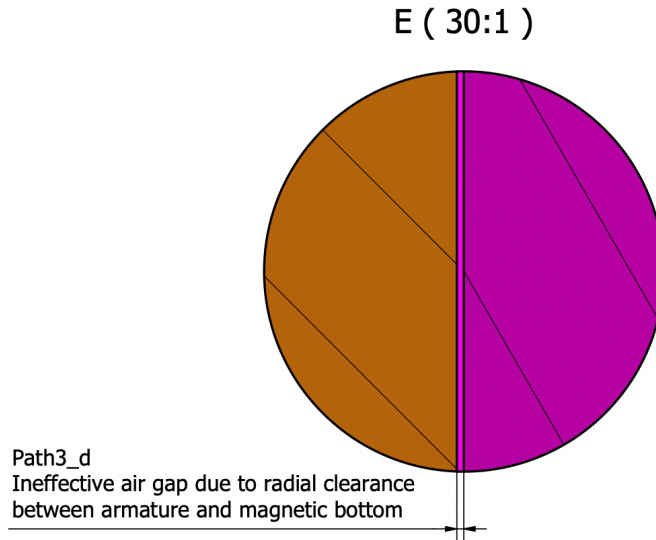
Figure 3.4: Detail view on horizontal air gap between magnetic bottom and armature.

$Path4_b$ is the path through the effective air gap shown in Fig. 3.5 where the use full magneto motive force is generated. $Path4_b$ is the vertical path through magnetic top. The effective air gap $Path4_b$ is further divided in to 2 sections. $Path4_{b1}$ is where opposing faces are horizontal and the magnetic flux through is vertical, therefore the

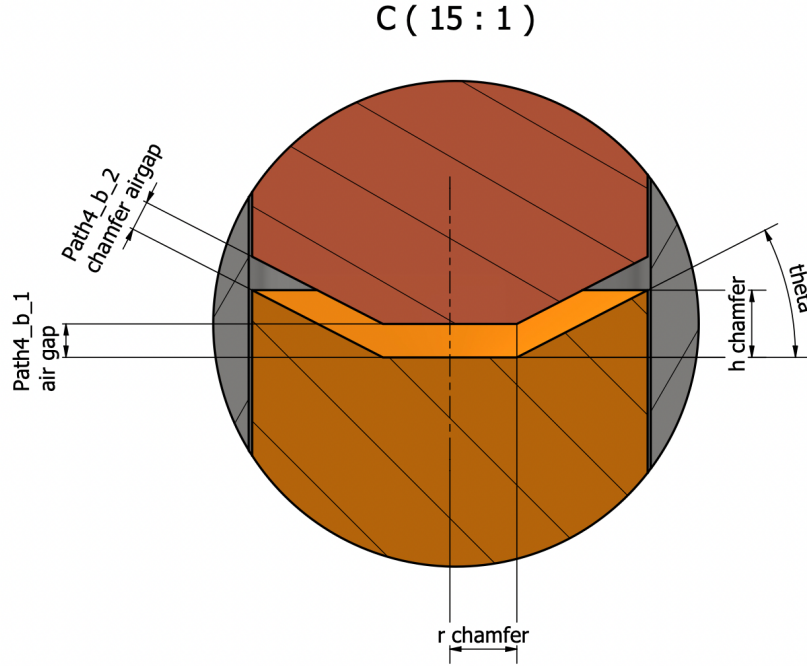Figure 3.5: Detail view on vertical effective air gap between magnetic top and armature.

magnetic reluctance of $Path4_{b1}$ is:

$$R_{Path4_{b1}} = \frac{h_{\text{air}}}{\mu_0 \, r_{\text{cham}}{}^2 \, \pi} \tag{3.4}$$

Computing $Path4_{b1}$ is trickier. First we compute

$$\theta = \text{atan}\left(\frac{h_{\text{cham}}}{r_A - r_{\text{cham}}}\right) \tag{3.5}$$

$$h_{chamferAirgap} = h_{air} \, cos(\theta) \tag{3.6}$$

and then we assumed that

$$A_{chamfer} = \pi \left(r_A{}^2 - r_{\text{cham}}{}^2\right) \tag{3.7}$$

When we apply the eq. 2.3 we compute $Path4_{b2}$ as the following:

$$R_{Path4_{b2}} = \frac{h_{\text{air}}}{\mu_0 \, \pi \left(r_A{}^2 - r_{\text{cham}}{}^2\right) \left(\frac{h_{\text{cham}}{}^2}{(r_A - r_{\text{cham}})^2} + 1\right)} \tag{3.8}$$

Total effective reluctance $Path4_b$ is computed with the following assumption for parallel magnetic flux in eq 3.9

$$\frac{1}{R_{combined}} = \frac{1}{R_1} + \frac{1}{R_2} + \cdots + \frac{1}{R_n} \tag{3.9}$$

$$\frac{1}{R_{combined}} = \frac{1}{R_{Path4_{b1}}} + \frac{1}{R_{Path4_{b2}}} \tag{3.10}$$

$Path4_b$ is computed and simplified in eq. 3.11.

$$
\begin{aligned}
R_{combined} &= \frac{1}{\frac{1}{R_{Path4_{b1}}} + \frac{1}{R_{Path4_{b2}}}} \\[2ex]
&= \frac{1}{\frac{\pi \, \mu_0 \, r_{\text{cham}}^2}{h_{\text{air}}} + \frac{\pi \, \mu_0 \, (r_A{}^2 - r_{\text{cham}}{}^2)\left(\frac{h_{\text{cham}}^2}{(r_A - r_{\text{cham}})^2} + 1\right)}{h_{\text{air}}}} \\[2ex]
&= \frac{h_{\text{air}} \left(r_A - r_{\text{cham}}\right)}{\mu_0 \, \pi \left(h_{\text{cham}}{}^2 \, r_A + r_{\text{cham}} \, h_{\text{cham}}{}^2 + r_A{}^3 - r_{\text{cham}} \, r_A{}^2\right)}
\end{aligned}
\tag{3.11}
$$

$$
\begin{aligned}
R_{Path4} ={}& \frac{c_a + \frac{h_C}{2} - h_{\text{air}} + t_{\text{cfa}} + \frac{t_{\text{mba}}}{2}}{\mu \, \mu_0 \, r_A{}^2 \, \pi} + \\[2ex]
& \frac{h_{\text{air}} \left(r_A - r_{\text{cham}}\right)}{\mu_0 \, \pi \left(h_{\text{cham}}{}^2 \, r_A + r_{\text{cham}} \, h_{\text{cham}}{}^2 + r_A{}^3 - r_{\text{cham}} \, r_A{}^2\right)} + \\[2ex]
& \frac{c_a + \frac{h_C}{2} + t_{\text{cfa}} + \frac{t_{\text{mta}}}{2}}{\mu \, \mu_0 \, r_A{}^2 \, \pi}
\end{aligned}
\tag{3.12}
$$

$$R_{total} = R_{Path1} + R_{Path2} + R_{Path3} + R_{Path4} \tag{3.13}$$

After computing the total reluctance we can compute the magnetic flux using the eq. 2.2 and the magneto motive force using the eq. 2.1.

Chapter 4

DYNAMIC MODEL OF A SOLENOID VALVE

4.1 Mechanical Model

The only moving part in this direct acting solenoid part is the armature. The normally closed solenoid valve is turned on and off via applying a voltage on the solenoid leads that creates the magneto motive force and lets the fluid flow through. In fig. 4.1 we present the forces acting on the armature. F_{mm} is the magneto motive force, F_{airgap} is the force generated by the fluid pressure in the air gap on the top surface of the armature, $F_{chamber}$ is the generated by the fluid pressure in the chamber on the bottom surface of the armature and F_{spring} is the force generated by the compression spring. This free body diagrams describes the dynamic behaviour of the valve. In section 2 we showed how to compute F_{mm} for a given design, armature
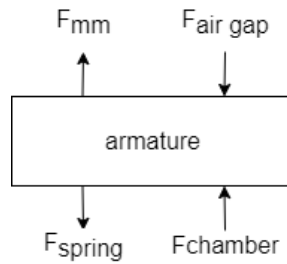

Figure 4.1: Armature Free Body Diagram

position and applied current.

$$F_{mm} = \frac{1 \cdot \phi^2}{2 \cdot \mu_0 \cdot S_2} \tag{2.1}$$

$$F_{airgap} = \pi \, r_A^2 \, P_{airgap} \tag{4.1}$$

$$F_{chamber} = \pi \, r_A^2 \, P_{chamber} \tag{4.2}$$

$$F_{spring} = (x + x_0) * k_s \tag{4.3}$$

where x_0 stands for the pre-loading of the spring and k_s is the spring constant

$$F(t) = F_{mm}(t) - F_{airgap}(t) + F_{chamber}(t) - F_{spring}(t) \tag{4.4}$$

$$F(t) = m\,\ddot{x}(t) \tag{4.5}$$

$$\dot{x}(t) = \dot{x}(t-1) + \ddot{x}(t-1)\,dt \tag{4.6}$$

$$x(t) = x(t-1) + \dot{x}(t-1)\,dt + \ddot{x}(t-1)\,dt^2 \tag{4.7}$$

The mass of the armature can be computed from the material density (430F SS for this model) ρ and the armature geometry.

$$m = r_A{}^2\,\rho\left(\frac{h_C}{2} + t_{\text{cfa}}\right) \tag{4.8}$$
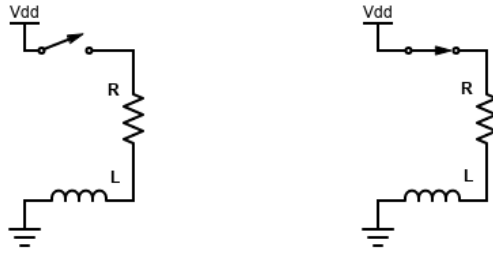
4.2   Electrical Model

Figure 4.2: Schematic of electrical circuit. (left) Valve powered off. (right) Valve powered on.

In fig. 4.2 the electrical schematic of the valve is presented. A solid state relay (SSR) is used to switch the solenoid on and off and any losses due to wiring and SSR is ignored in the model. We can represent the schematic with the following equations:

$$\begin{aligned} V_{dd} &= V_L + V_R \\ &= L\,di + R\,i \end{aligned} \tag{4.9}$$

$$V_{dd} = L(t)\,\frac{di}{dt}(t) + R\,i(t) \tag{4.10}$$

Assuming V_{dd} is constant we can compute $\frac{di}{dt}$ with the following derivation:

$$V_L(t) = V_{dd} - R\,i(t) \tag{4.11}$$

$$\frac{di}{dt}(t) = \frac{V_L(t)}{L(t)} \tag{4.12}$$

We can compute the inductance of the solenoid system using the eq. 4.13. Inductance will play a crucial role in the dynamic analysis of the solenoid valve. Inductance will dictate the reaction time of the solenoid valve.

$$L = \frac{N\,\phi}{i} = \frac{N^2}{R_{total}} \tag{4.13}$$

We can compute the resistance R from coil geometry (R_{Cin} coil inner radius, R_{Cout} coil outer radius), winding number N, wire diameter d_w and electrical resistivity of the conductor ρ as follows:

$$R = \pi\,(r_{Cout} + r_{Cin})\,N\,\rho \tag{4.14}$$

Finally we can compute $i(t)$ with the follwing equation:

$$i(t) = i(t-1) + \frac{di}{dt}(t-1)\,dt \tag{4.15}$$

Notice in fig. 4.2 that the circuit is a LR circuit. Valve reaction time is an important
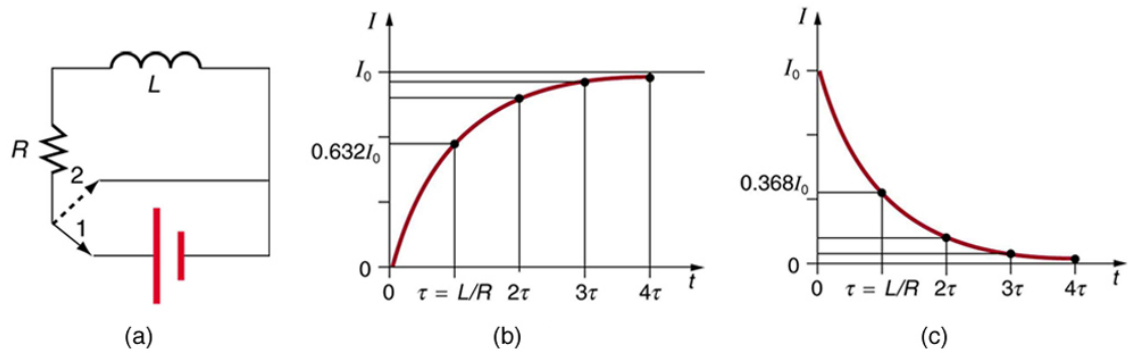

Figure 4.3: (a) An RL circuit with a switch to turn current on and off. When in position 1, the battery, resistor, and inductor are in series and a current is established. In position 2, the battery is removed and the current eventually stops because of energy loss in the resistor. (b) A graph of current growth versus time when the switch is moved to position 1. (c) A graph of current decay when the switch is moved to position 2.[OpenStax, 2022]

performance metric for solenoid valves. Generally it is assumed that 3τ is the time that the valve is fully opened. Valve closing time on the other hand depends on the spring constant k_s and pressure balance between chamber and air gap. This will be discussed in the next section

$$\tau = \frac{L}{R} \tag{4.16}$$

Notice in eq. 4.13 inductance varies with magnetic flux, thus varies by R_{total}. This results in different time constants for different armature positions. For this dynamic model, a positive voltage will be applied for $1.2\,\tau_{opening}$ seconds. After this duration the voltage will be removed and the simulation will be run for another $1.2\,\tau_{closing}$ seconds.

$$\tau_{opening} = \frac{L(h_{air})}{R} \tag{4.17}$$

$$\tau_{opening} = \frac{L(c_a)}{R} \tag{4.18}$$

In eq. 4.17 the inductance is computed with the maximum air gap and in eq. 4.18 the inductance is computed with minimum air gap that is equal to the axial clearance c_a.

4.3   Simulation Meta Data

Simulation time step is set to $10ns$, $10^{-8}s$, in order to account for the dynamic nature of the simulation. As it is presented in the next section, mass flows and the change in pressures and temperatures are integrated through the simulation. A small time step is required to keep the simulation stable. For step sizes above $1us$ the simulation diverges due to small control volumes and high flow rates.

4.4   Flow Model

The valve design has 2 control volumes. These control volumes are V_{airgap} and $V_{chamber}$. The states of these volumes are defined by their volume V, temperature T, density ρ and mass M. The interaction between these control volumes are defined

by the armature radial clearance flow path. This flow path is defined by a flow cross section area A_{rc} and a discharge coefficient $C_{d,rc}$.

The valve is placed between two reservoirs, upstream and downstream. For this model the upstream and downstream reservoirs are assumed to be infinite and have constant temperature and density. The interaction between the chamber and the reservoirs are defined by inlet and outlet orifices. These orifices are defined by r_{inlet}, $C_{d,inlet}$, r_{outlet} and $C_{d,outlet}$. Outlet orifice is open gradually due to the mechanics of the armature. This is taken in to account by multiplying the effective area with the armature travel percentage.
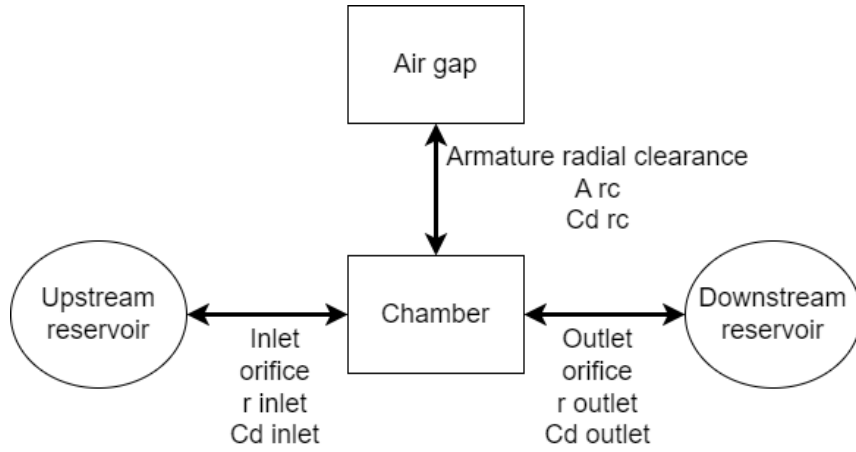

Figure 4.4: Abstraction of valve volumes, and flow paths.

The following subsections will present the simulation algorithm in the order of execution for each loop.

4.4.1 Armature Motion

The armature motion is computed with the forces computed in the previous loop with order: eqs. 4.5, 4.6, 4.7. After computing this loops position, velocity and acceleration; if they exceed the range of motion position is capped and velocity and acceleration is set to zero.

4.4.2 Electrical and Magnetic Circuit Simulation

The electrical current for this loop is computed with eq. 4.15. The applied voltage is calculate based on the time in the simulation mentioned in eqs 4.17 and4.18. R_{total} is computed with the current armature position and used to calculate current flux with eq. 2.2. F_{mm} is computed with eq. 2.1. Inductance voltage V_L and change in electrical current for next step $\frac{di}{dt}$ is computed with eqs. 4.11 and 4.12.

4.4.3 Control Volume Changes

Volume of the air gap and the chamber changes due to armature translation. This changes the temperature and the pressure in these control volumes. These processes are assumed to be adiabatic compression/expansion because the volume changes happen under in the order of us.

$$P(i) = P(i-1) \left(\frac{V(i-1)}{V(i)} \right)^{\gamma} \tag{4.19}$$

$$T(i) = T(i-1) \left(\frac{V(i-1)}{V(i)} \right)^{(\gamma-1)} \tag{4.20}$$

4.4.4 Gas Flows

The order of gas flow computation is from downstream to upstream. First the mass flow from chamber to downstream reservoir $\dot{m}_{c,d}$ and its effects on the $M_{chamber}$, $P_{chamber}$ and $T_{chamber}$ are computed. Then the mass flow between chamber and air gap $\dot{m}_{c,a}$ and its effects on $M_{chamber}$, $P_{chamber}$ $T_{chamber}$, M_{airgap}, P_{airgap} and T_{airgap} are computed. Finally the mass flow from upstream reservoir to chamber $\dot{m}_{u,c}$ and its effects on the $M_{chamber}$, $P_{chamber}$ and $T_{chamber}$ are computed.

Computing Flow Velocity

$$M = \sqrt{ \left(\frac{P_{high}}{P_{low}} \right)^{\left(\frac{\gamma-1}{\gamma} \right)} \frac{2}{\gamma-1} } \tag{4.21}$$

Flow velocity between two pressure reservoirs is computed by the eq. 4.21 derived from the adiabatic flow equation [NASA, 2021]. If the resulting Mach number M is greater than 1, it is capped to 1 because the flow through orifices is choked.

Computing Mass Flow Rate

After computing flow velocity M one can compute the mass flow rate $\dot{m}$ using the eq. 4.22 [NASA, 2021], where A is the orifice surface area, P_t is the total/upstream pressure, T_t is the total/upstream temperature, R is the gas constant and γ is the ratio of specific heats for the gas.

$$\dot{m} = \frac{A\,P_t}{\sqrt{T_t}}\,\sqrt{\frac{\gamma}{R}}\,M\left(1 + \frac{\gamma - 1}{2}\,M^2\right)^{-\frac{\gamma+1}{2(\gamma-1)}} \tag{4.22}$$

Computing Gas Charge/Discharge

After computing the mass flow rate $\dot{m}$ between two control volumes/reservoirs, the new mass M, pressure P and temperature T should be computed for the control volumes.

$$\Delta m = \dot{m}\,dt = M(i) - M(i-1) \tag{4.23}$$

$$M(i) = M(i-1) + \Delta m \tag{4.24}$$

To compute the next state of the control volumes it is assumed that the process is adiabatic. Thus we can write the following energy and mass conservation.

$$\Delta m = M(i) - M(i-1) \tag{4.25}$$

$$\Delta e = M(i)\,u(i) - M(i-1)\,u(i-1) = \Delta m\,h \tag{4.26}$$

$$0 = \Delta m\,h - M(i)\,u(i) + M(i-1)\,u(i-1)$$

$$0 = \Delta m\,C_p\,T_{\Delta m} - M(i)\,C_v\,T(i) + M(i-1)\,C_v\,T(i-1) \tag{4.27}$$

$$0 = \Delta m\,\gamma\,T_{\Delta m} - M(i)\,T(i) + M(i-1)\,T(i-1)$$

Eq. 4.27 leverages the fact that $\gamma = \frac{C_p}{C_v}$ to simply the expression.

$$T(i) = \frac{\gamma\,\Delta m\,T_{\Delta m} + M(i-1)\,T(i-1)}{M(i)} \tag{4.28}$$

$$P(i) = P(i-1)\left(\frac{T(i)}{T(i-1)}\right)^{\frac{\gamma}{\gamma-1}} \tag{4.29}$$

Control volume states are computed with the equations above.

Computing Forces on Armature

Last step of the simulation loop is to compute the forces acting on the armature. These forces are computed with the eqs. 2.1, 4.1, 4.2, 4.3 and 4.4.

4.5 Results

Simulation is set with the following parameters:

$c_r = 0.1mm$

$c_a = 0.1mm$

$h_C = 50mm$

$r_{Cout} = 15mm$

$D_w = 0.27mm$

$t_{cfr} = 1.5mm$

$t_{cfa} = 5mm$

$t_{mba} = 5mm$

$t_{mta} = 5mm$

$r_A = 4.9mm$

$r_{cham} = 2mm$

$h_{cham} = 2mm$

$t_{shell} = 2mm$

$PR = 0.9$

$CSF = 0.75$

$h_a ir = 1mm$

$\mu = 850$

$\mu_0 = 1.25663706212 \cdot 10^{-6} \, H/m$

$CWCC = 10 \cdot 10^6 \, A/m^2$

$erc = 1.68 \cdot 10^{-8} \, \Omega \, m$

$t_{powered\,on} = 1.2 \, \tau_{open}$

$t_{powered\,off} = 1.2 \, \tau_{close}$
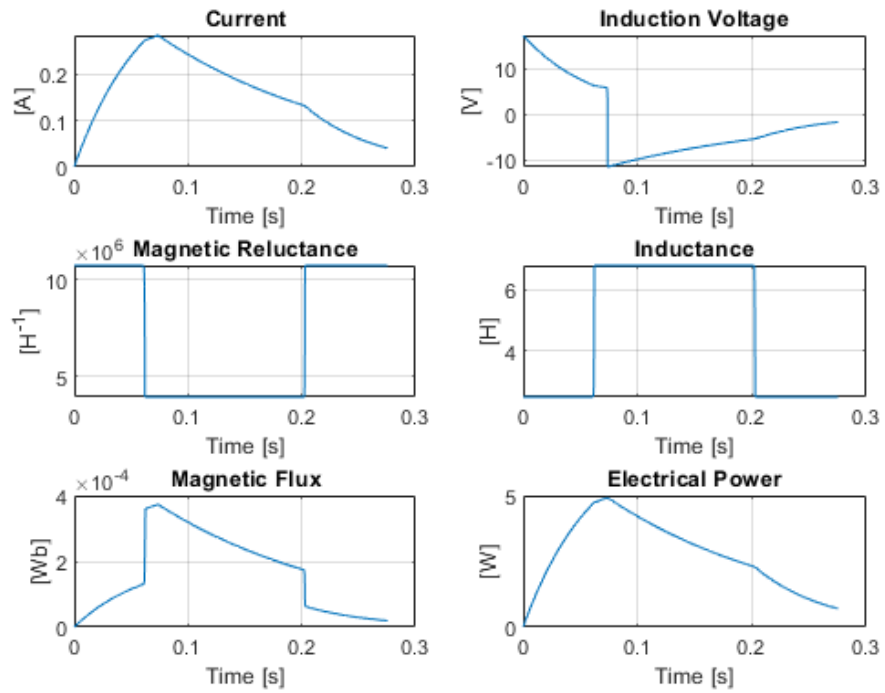
Figure 4.5: Electrical and magnetic circuit development over time.
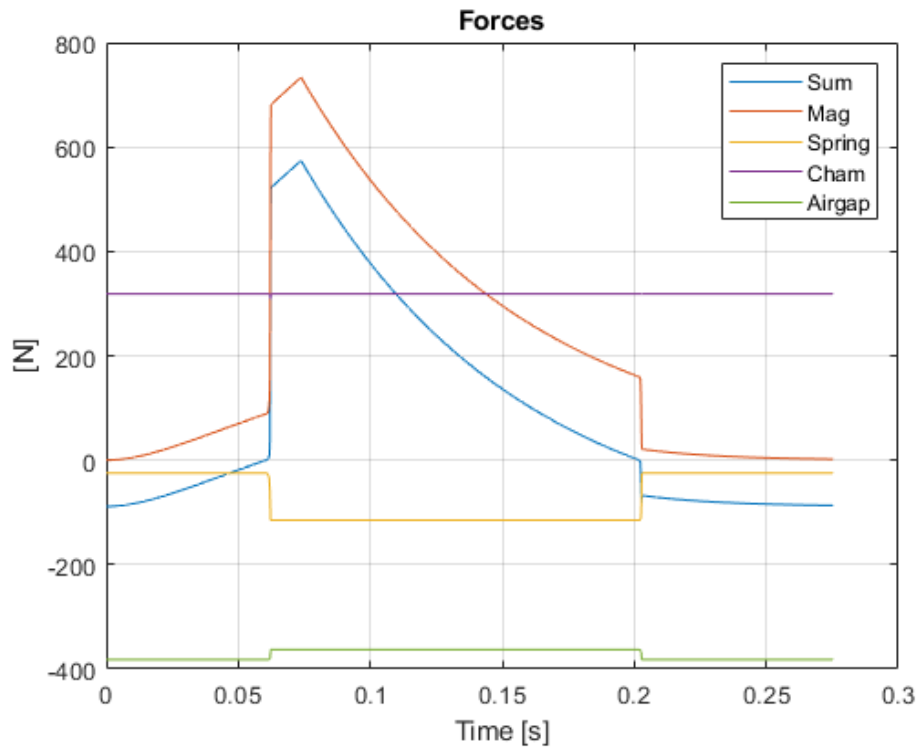
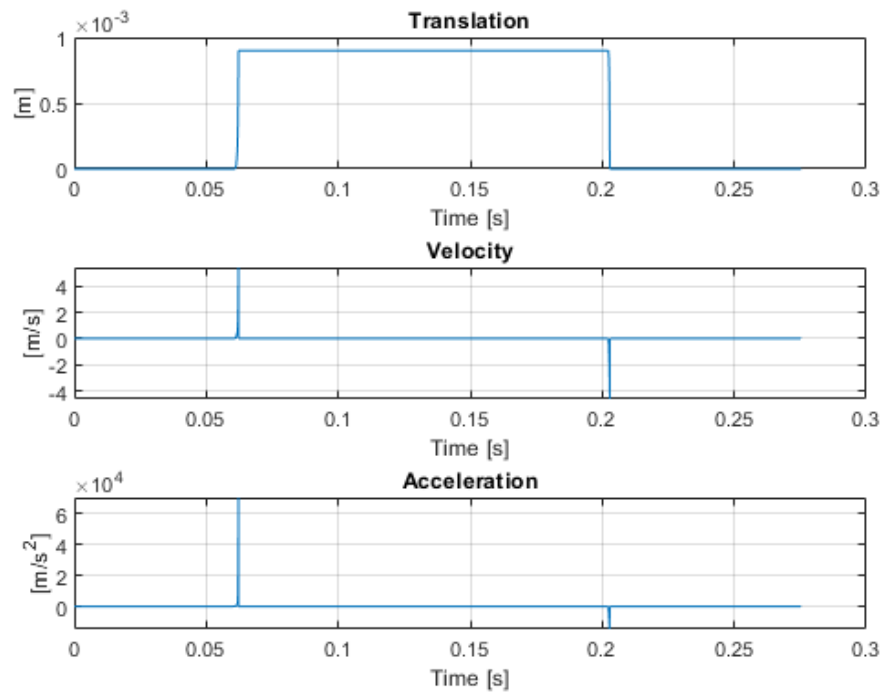Figure 4.6: Forces acting on the armature.
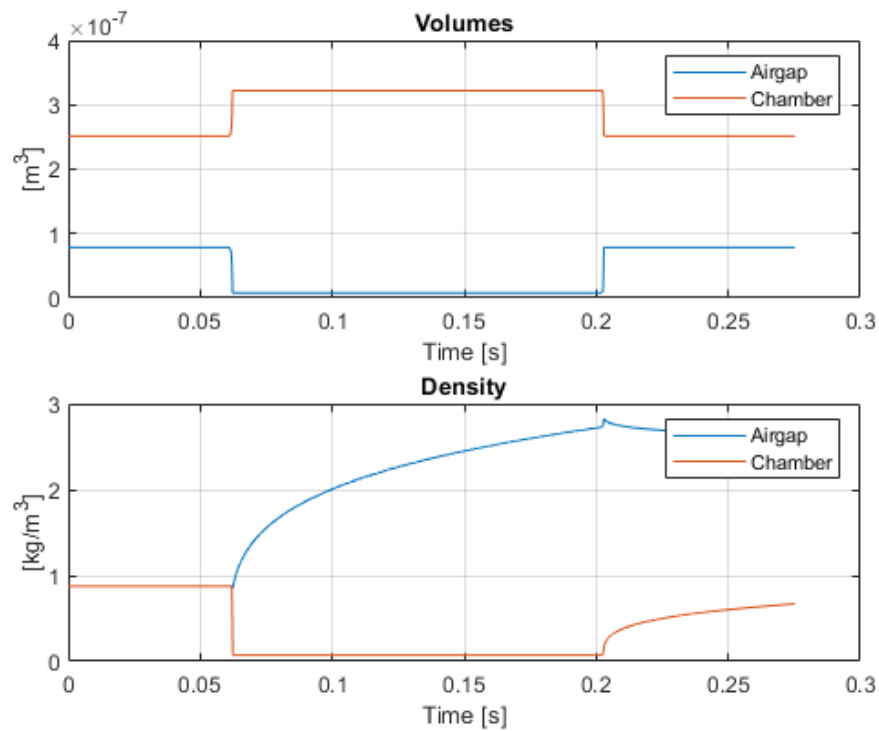
Figure 4.7: Motion on the armature.
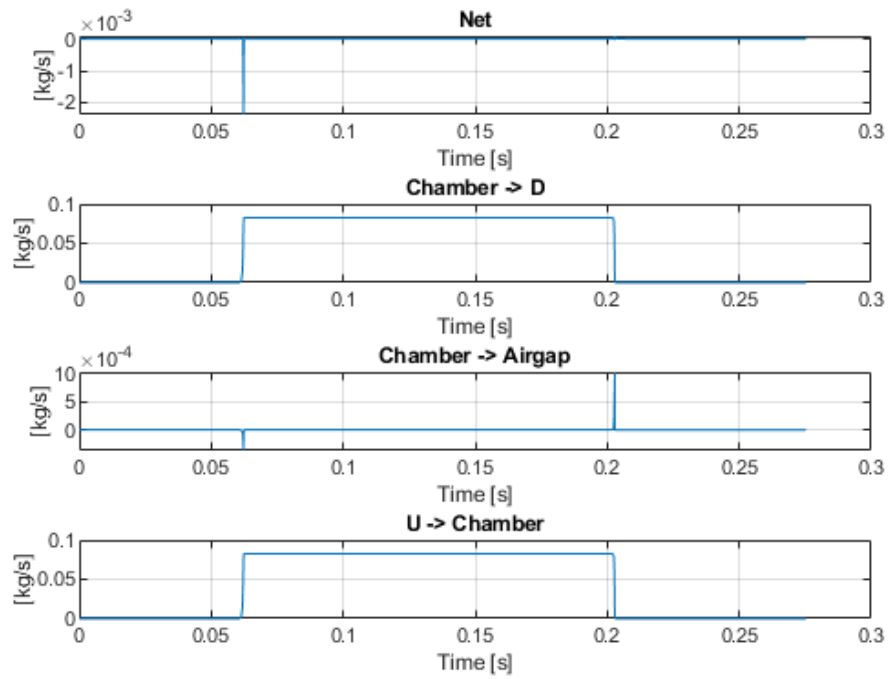

Figure 4.8: Change of the volume

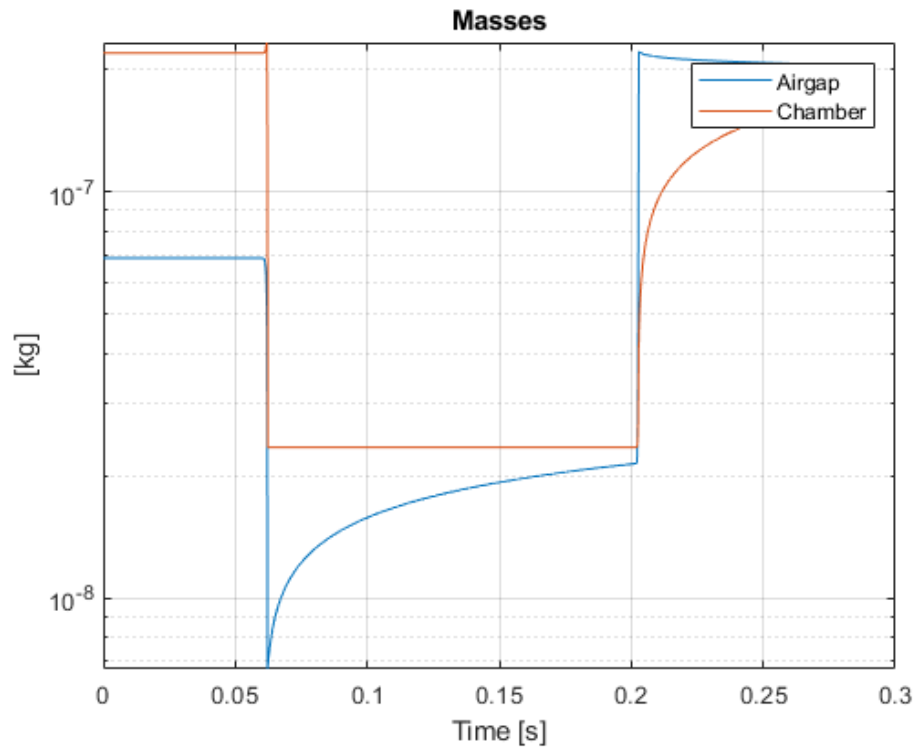Figure 4.9: Mass flows to and from control volumes.
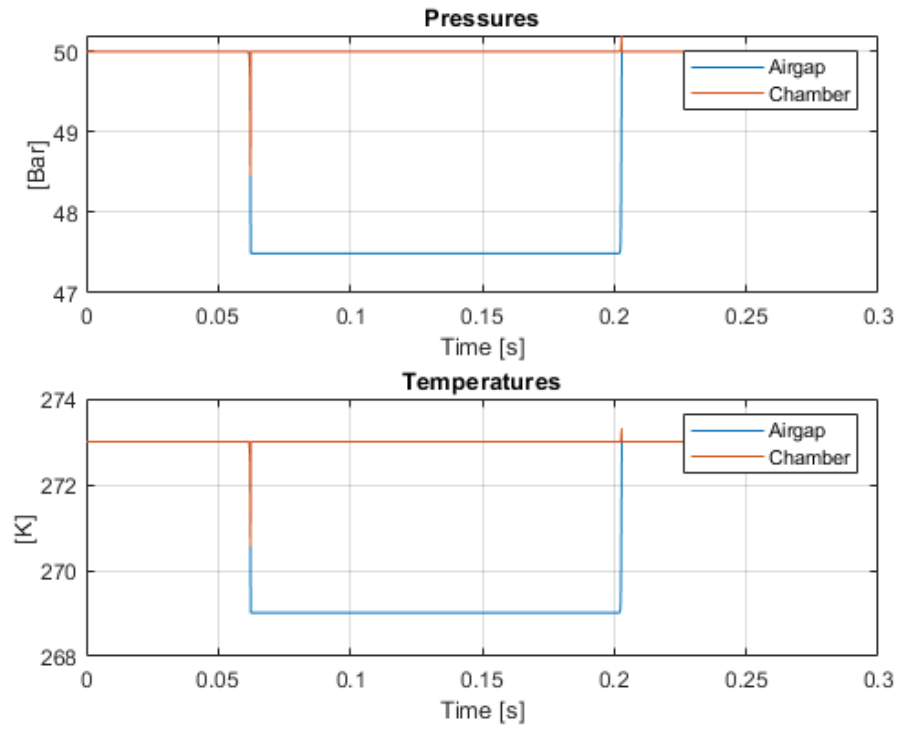

Figure 4.10: Change of the mass

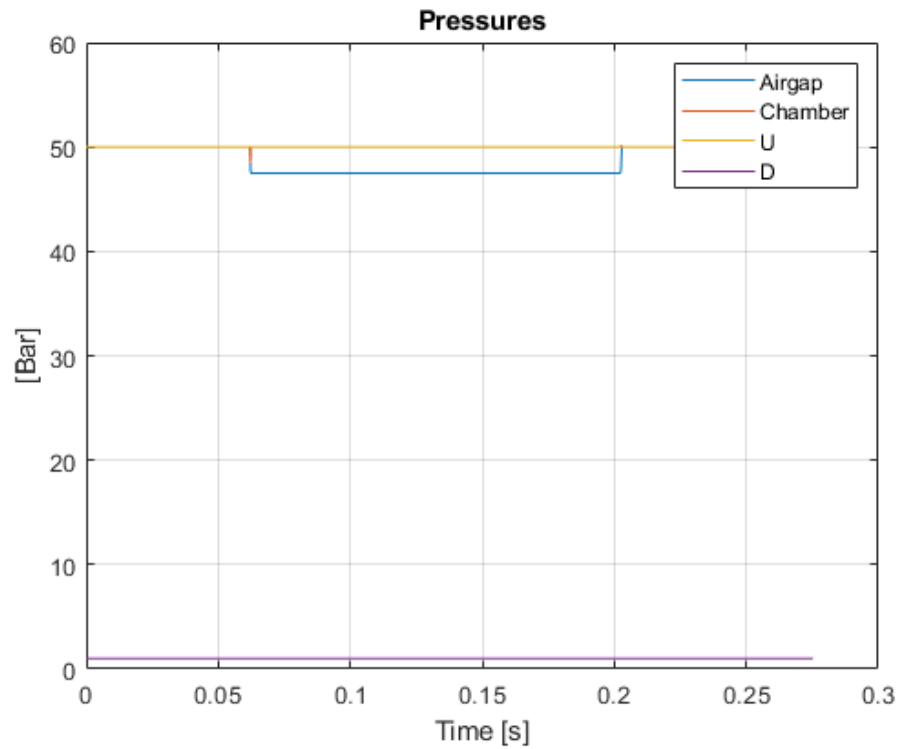Figure 4.11: Control volume pressure and temperature

Figure 4.12: Pressures of control volumes and reservoirs.

Chapter 5

DISCUSSION